ARTICLE　OPEN

Field-induced metal-to-insulator transition and colossal anisotropic magnetoresistance in a nearly Dirac material EuMnSb$_2$

Z. L. Sun[1,6], A. F. Wang [2,6], H. M. Mu[1], H. H. Wang[1], Z. F. Wang [1], T. Wu[1], Z. Y. Wang[1], X. Y. Zhou [2✉] and X. H. Chen [1,3,4,5✉]

Realizing applicably appreciated spintronic functionalities basing on the coupling between charge and spin degrees of freedom is still a challenge. For example, the anisotropic magnetoresistance (AMR) effect can be utilized to read out the information stored in magnetic structures. However, the application of AMR in antiferromagnet-based spintronics is usually hindered by the small AMR value. Here, we discover a colossal AMR with its value reaching 1.84×10^6% at 2 K, which stems from the field-induced metal-to-insulator transition (MIT), in a nearly Dirac material EuMnSb$_2$. Density functional theory calculations identify a Dirac-like band around the Y point that depends strongly on the spin–orbit coupling and dominates the electrical transport. The indirect band gap at the Fermi level evolves with magnetic structure of Eu^{2+} moments, consequently giving rise to the field-induced MIT and the colossal AMR. Our results suggest that the antiferromagnetic topological materials can serve as a fertile ground for spintronics applications.

INTRODUCTION

The manipulation of charge transport by spin degree of freedom in solid-state systems is at the core of spintronics. Recently, antiferromagnets have generated significant interest in the field of spintronics owing to their enriched properties, such as zero stray magnetic field, ultrafast spin dynamics, and remarkable rigidity against external fields[1–4]. Anisotropic magnetoresistance (AMR), which is defined as the dependence of the resistivity on the direction of the magnetization with respect to current or crystal axes, could be utilized as electrical-readout to detect the switch of magnetization in antiferromagnet (AFM)-based spintronic devices. AMR-based memory effects have been successfully demonstrated in several antiferromagnets, such as FeRh[5] and MnTe[6], opening perspective for both fundamental research and device technology of AFM spintronics[5–11]. In principle, the conventional AMR effect, in which the electronic band structure is dependent on the spin orientation, is mainly associated with the magnetocrystalline anisotropy arising from the relativistic spin–orbit coupling (SOC). In this sense, the SOC-induced anisotropic response of band structure to external magnetic field and the detailed position of the Fermi level determine the AMR in practical antiferromagnets[12–15]. However, experimentally observed AMR is always limited to a few hundred percent, which is much smaller than the giant magnetoresistance (GMR)[16,17] or tunneling magnetoresistance (TMR), hindering its further practical application. Thus, the hunt for new materials with large AMR and new strategies toward enhancement of AMR are highly desired.

On the other hand, the rise of the magnetic topological materials provides a new fertile playground to explore the manipulation of quantum transport phenomena by spin degrees of freedom[2]. In recent years, the strong correlation between

magnetism and topological band structure has been widely discussed in magnetic topological materials[18,19]. Especially, the topological band structure can be strongly dependent on the strength of SOC and the detailed magnetic structure in some magnetic topological materials[20–22], which leads to anisotropic response of band structure near the Fermi level to the change of magnetic structure. Therefore, the magnetic topological materials can potentially generate a large AMR, which has not yet been observed experimentally. Among various magnetic topological materials, the family of AMnPn_2 (A = Ca, Sr, Ba, Eu or Yb, Pn = Sb or Bi) materials, in which the conducting two-dimensional (2D) Bi/Sb layers separated by the insulating Mn-Pn layers with magnetism can host Dirac-like fermions, exhibits great potential for strong correlation between the Dirac-like band structure and magnetism. In principle, the 2D Bi/Sb layers with square net structure can host 2D Dirac-like fermions[23,24], and quasi-2D massive Dirac-like fermions with SOC gap have been observed in AMnPn_2 with Bi/Sb square net[23,25–31], including SrMnBi$_2$[23,25] and CaMnBi$_2$[26]. On the other hand, although theoretical study[32] has argued that the formation of zigzag chain structure in 2D Bi/Sb layers will destroy the linear band dispersion held by the square net structure, the existence of nontrivial Dirac fermions have also been verified in the AMnPn_2 family materials with zigzag chain structure by quantum oscillation experiments, including SrMnSb$_2$[33], CaMnSb$_2$[34], and BaMnSb$_2$[35,36]. Angle-resolved photoemission spectroscopy (ARPES) experiments have further confirmed a linearly Dirac-like dispersive band structure around Fermi level in BaMnSb$_2$[35,36], EuMnSb$_2$[37], and CaMnSb$_2$[38]. These results strongly indicate that holding a Dirac-like dispersion seems to be a generic nature of band structure in the AMnPn_2 family materials. More interestingly, a considerable coupling between the

---

[1]Hefei National Laboratory for Physical Sciences at Microscale and Department of Physics, and Key Laboratory of Strongly-Coupled Quantum Matter Physics, Chinese Academy of Sciences, University of Science and Technology of China, Hefei, Anhui 230026, China. [2]Center for Quantum Materials and Devices and Chongqing Key Laboratory of Soft Condensed Matter Physics and Smart Materials, College of Physics, Chongqing University, Chongqing 401331, China. [3]CAS Center for Excellence in Superconducting Electronics (CENSE), Shanghai 200050, China. [4]CAS Center for Excellence in Quantum Information and Quantum Physics, Hefei, Anhui 230026, China. [5]Collaborative Innovation Center of Advanced Microstructures, Nanjing University, Nanjing 210093, China. [6]These authors contributed equally: Z. L. Sun, A. F. Wang. ✉email: xiaoyuan2013@cqu.edu.cn; chenxh@ustc.edu.cn

magnetism and the Dirac-like fermions in the conducting Bi/Sb layer has been clearly observed by neutron-scattering and Raman-scattering measurement[39–42] in various $AMnPn_2$ family materials. Especially, when A represents magnetic ion Eu^{2+}, the interaction between local moments and itinerant carrier could be significantly enhanced due to the highly tunable magnetic moments of Eu^{2+} by external magnetic field. For instance, quantum Hall effect is observed in bulk antiferromagnet $EuMnBi_2$, in which the field-controlled Eu^{2+} magnetic order suppresses the interlayer coupling[28]. In contrast to the positive magnetoresistance (MR) observed in other members of this family, $EuMnSb_2$ with zigzag chain structure in 2D Sb layers shows a large negative MR, especially for the temperature range below the AFM ordering temperature of Eu^{2+} moments[37,43,44]. All these results strongly suggest a strongly modulated Dirac-like band structure by the magnetism of Eu^{2+} moments in the $EuMnPn_2$ materials.

Here, we discover a colossal AMR effect during the field-induced metal-to-insulator transition (MIT) in a nearly Dirac material $EuMnSb_2$ with an AFM order of Eu^{2+} moments. The colossal AMR reaches $1.84 \times 10^6\%$ at 2 K, which is four orders of magnitude larger than previously reported values in antiferromagnets. Our density functional theory (DFT) calculations indicate that the field-induced MIT and colossal AMR effect are related to a Dirac-like band structure around Y point, which is strongly modulated by SOC and antiferromagnetism.

RESULTS
Magnetic and transport properties
$EuMnSb_2$ crystallizes in an orthorhombic structure with space group $Pnma$ (No. 62) as shown Fig. 1d. The X-ray diffraction (XRD) pattern shows high quality of our sample with lattice parameter $a = 22.56$ Å (shown in Supplementary Fig. 1), which is consistent with the previous report[37,43,44]. The Mn sublattice, sandwiched by two Sb atomic layers, exhibits C-type AFM order with magnetic moments aligned along the a axis below ~346 K[37,44]. So far, there

is a discrepancy between the reported magnetic structures of Eu sublattice below 21 K. A-type AFM structure with magnetic moments along the c axis was suggested by powder neutron diffraction measurements[37], while neutron diffraction refinements performed on single crystals have found a canted A-type AFM order with Eu^{2+} moments lying 41° away from the a axis in the ac plane[44]. To confirm the magnetic order of Eu sublattice in our $EuMnSb_2$ single crystal, we have performed magnetization measurements. The temperature-dependent magnetic suscept-ibilities χ_a and χ_{bc} are displayed in Fig. 1a, with magnetic field (H) applied along the a axis and bc plane, respectively. χ_a shows a clear kink at 21 K, denoting the formation of AFM order of Eu sublattice. In Fig. 1b, we display the isothermal magnetization of $EuMnSb_2$ with magnetic field applied along the a axis and bc plane at 2 K, respectively. In both cases, the magnetization does not saturate up to 7 T. When H is applied along the a axis, a spin-flop transition is observed at $H = 1.5$ T (red curve), consistent with the previous report[43]. The magnetization along the a axis is slightly smaller than that in the bc plane, indicating that the magnetic moments of Eu^{2+} are more easily polarized in the bc plane. The small anisotropy of magnetization between the a axis and bc plane implies a preferred canted A-type AFM structure of Eu^{2+} moments in $EuMnSb_2$ as shown in Fig. 1d. As we will discuss later, our DFT calculations also find that the total energy with canted A-type AFM structure of Eu^{2+} moments is smaller than that with A-type AFM structure. Therefore, we consider the canted A-type AFM order as the magnetic ground state of Eu sublattice in the relevant discussion of the present paper. More magnetic susceptibility data can be found in Supplementary Fig. 2.

Figure 1c shows temperature dependence of in-plane resistivity ρ_{xx} for $EuMnSb_2$ with external magnetic field applied along the a axis. At zero field, it shows a semiconducting behavior with a kink appearing at the AFM transition temperature of the Eu sublattice ($T_N \sim 21$ K). The resistivity ρ_{xx} at zero magnetic field can be fitted by the Arrhenius equation $\rho_{xx}(T) \propto \exp(E_A/2k_BT)$ from 200 to 300 K, where E_A is the thermal activation energy and k_B is the
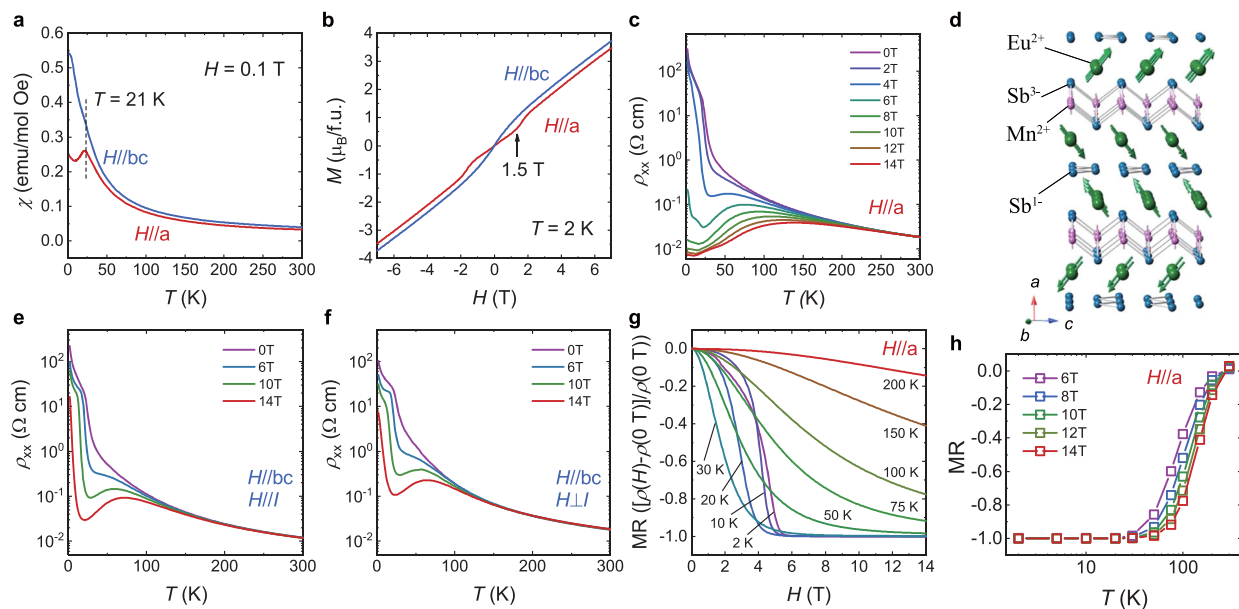

Fig. 1 Resistivity, magnetoresistance, and susceptibility of EuMnSb₂. a Temperature dependence of susceptibilities χ_a and χ_{bc} with magnetic field of 0.1 T applied along the a axis and bc plane. **b** Isothermal magnetizations of $EuMnSb_2$ with magnetic field paralleled to the a axis and bc plane at 2 K. **c** Temperature-dependent in-plane resistivity with magnetic fields applied along the a axis. **d** Schematic illustration of the magnetic structure of $EuMnSb_2$ at zero magnetic field. Eu sublattice forms canted A-type AFM order and Mn sublattice forms C-type AFM order. **e** Temperature-dependent in-plane resistivity ρ_{xx} under different magnetic fields in the bc plane. The magnetic field is parallel to the current direction. **f** Temperature-dependent in-plane resistivity ρ_{xx} under different magnetic fields in the bc plane. The magnetic field is perpendicular to the current direction. **g** MR (defined as MR = $[\rho_{xx}(H)-\rho_{xx}(0\,T)]/\rho_{xx}(0\,T)$) of $EuMnSb_2$ at varying temperatures with magnetic field along the a axis. **h** MR as a function of temperature with magnetic fields applied along the a axis.

Boltzmann constant (shown in Supplementary Fig. 3). The fitting procedure gives an activation energy of 75.9 meV which is larger than that in the previous report[43]. The resistivity behavior below T_N cannot be fitted by the thermal activation model, just like the cases in many of the narrow-gap semiconductors. This implies that other contributions might also need to be taken into account to explain the electrical transport properties at low temperature, such as the hopping transport that stems from in-gap impurity levels. Besides, the spin fluctuation of local Eu^{2+} moments below 200 K may affect the electrical transport as well. We note that the resistivity of our $EuMnSb_2$ sample at zero magnetic field shows insulating behavior below T_N, which is quite different from that in the previous report exhibiting a dip below T_N[37,43]. In addition, the value of resistivity in our $EuMnSb_2$ sample is also much larger than that in previously reported sample[37,43,44]. We ascribe the insulating behavior of resistivity to a lower carrier density in our $EuMnSb_2$ sample, thus making the Fermi level locate inside the band gap. This will be discussed below in detail. When H is applied along the a axis, it induces a MIT at low temperature in our $EuMnSb_2$ sample. With increasing magnetic field, the small kink in resistivity corresponding to T_N moves to lower temperature and the upturn behavior below T_N becomes weak with increasing magnetic field. This indicates that the band gap below T_N decreases under magnetic field, which is consistent with the following band structure calculations. The resistivity ρ_{xx} with the magnetic field perpendicular and parallel to the current direction in the bc plane is shown in Fig. 1e, f, respectively. ρ_{xx} with $H//bc$ shows relatively weak negative MR behavior and remains with insulating behavior at low temperature even at 14 T, which is quite different from the nearly metallic behavior with $H//a$.

The magnetic-field-dependent resistivity data shown in Fig. 1c reveals that $EuMnSb_2$ exhibits a remarkable negative MR response at low temperatures. To proceed, we define MR as MR = $[\rho_{xx}(H) - \rho_{xx}(0\,T)]/\rho_{xx}(0\,T)$ and display the MR at different temperatures with magnetic field applied along the a axis in Fig. 1g. The MR has been symmetrized with respect to positive and negative magnetic fields to remove the Hall contribution. $EuMnSb_2$ shows a large negative MR below T_N and above about 5 T. The negative MR behavior weakens with temperature increasing above T_N. A large negative MR with a maximum value of -99.9987% at 2 K and under $H = 14\,T$ is observed, which is larger than the value in previously reported $EuMnSb_2$ by far[37,43]. To gain more sight into the emergence of the negative MR, we have plotted the temperature-dependent MR at various magnetic fields applied along the a axis in Fig. 1h. The large negative MR response sets in when the magnetic moments of Eu^{2+} form AFM order, and disappears quickly above T_N, indicating a clear correspondence between the negative MR and magnetic order of Eu sublattice. Previously, negative MR has been observed in some low-carrier-density magnetic Eu-based materials[45–48]. The negative MR was ascribed to the formation of magnetic polaron, for example, in $Eu_5In_2Sb_6$[47] and EuB_6[48]. Nevertheless, ac magnetic susceptibility measurement in $EuMnSb_2$[43] does not support the existence of magnetic polaron, which excludes the magnetic polaron as possible origin of the negative MR. Instead, the germane correlation between the charge transport and magnetization implies that the large negative MR observed in $EuMnSb_2$ is related to the magnetic order of Eu^{2+} moments, which can be further demonstrated by the following band structure calculations.

Anisotropic magnetoresistance
Conspicuously, the MR is also extremely anisotropic when the magnetic field rotates from the a axis, as shown in Fig. 2a. The setup geometry of our measurements is illustrated in the inset of Fig. 2a. Here the electric current I is applied in the bc plane while magnetic field H is rotated from the a axis by angle θ with keeping perpendicular to I. All curves with varied angles show a negative

MR, and the resistivity at high field increases drastically with θ increasing. Figure 2b displays the AMR = $[\rho_{xx}(\theta) - \rho_{xx}(0°)]/\rho_{xx}(0°)$[49,50] as a function of θ at 2 K under several representative magnetic fields. It clearly shows a remarkably large AMR with maximum value $1.84 \times 10^6\%$ at 12 T, which exceeds previously reported AMR values in AFM materials by far. A complete AMR contour map with magnetic field larger than 5 T is presented in Fig. 2c. The AMR shows two-fold symmetry and the center located at $H = 12\,T$ and $\theta = 90°$. Figure 2d displays the magnetic-field-dependent AMR at 90°, and one can see that the AMR shows a relatively small value below 5 T, above which it increases rapidly and shows the maximum at 12 T. The AMR data at low magnetic fields are shown in Supplementary Fig. 4. In fact, the relatively smaller AMR value at 5 T already reaches ~800%.

To reveal the temperature dependence of the colossal AMR, we have measured the AMR at various temperatures under $H = 12\,T$, as depicted in Fig. 2e. The two-fold AMR decreases monotonically with increasing temperature. Figure 2f shows the temperature-dependent AMR value at $H = 12\,T$ and $\theta = 90°$. The AMR rapidly decreases with increasing temperature to T_N, and shows a much smaller value above T_N. It further implies a close relation between the colossal AMR and the AFM order of Eu^{2+} moments. When the magnetic field is rotated in the bc plane, it shows relatively small AMR, as displayed in Supplementary Fig. 5.

Electronic structure calculations
To investigate the origin of the colossal AMR and the topological nature of our $EuMnSb_2$ sample, we have calculated the electronic band structure with different Eu^{2+} magnetic orders. First, we performed the band structure calculation of $EuMnSb_2$ in the AFM state of Eu sublattice without SOC (Fig. 3a). The band structure at Y point shows a linear band dispersion with a tiny gap, indicating $EuMnSb_2$ is a massive Dirac semimetal without considering SOC, just similar to the other members in the $AMnPn_2$ family. Next, we performed band structure calculations considering canted A-type AFM and c-axis-oriented A-type AFM orders of Eu sublattice with SOC, as shown in Fig. 3b, c, respectively. The resulted total energy in the former case is about 10 meV less than that in the latter, indicating that the Eu sublattice in $EuMnSb_2$ favors the canted A-type AFM order at zero magnetic field. As mentioned earlier, this finding is consistent with our magnetic susceptibility measurements.

Our band structure calculation reveals a strong SOC effect at Y point. Due to the effect of SOC, the band structure at Y point opens a sizable gap with 162 meV for canted A-type AFM order of Eu sublattice and 146 meV for c-axis-oriented A-type AFM order of Eu sublattice. Despite the existence of band gap, the band structure shows a highly dispersive and linear band at Y point, manifesting $EuMnSb_2$ is a nearly Dirac semimetal with a gapped Dirac point. The states near the Fermi level mainly comes from the 2D Sb zigzag layer (as shown in Supplementary Fig. 6), which indicates the charge carriers in Sb layers are Dirac-like and highly sensitive to SOC effect. We can understand the generation of the gapped Dirac point at Y point from the orthorhombic distortion from the Sb tetragonal square. For tetragonal $AMNPn_2$ with Sb/Bi square net, the Dirac-like band exists along the Γ–M line[23,24,51]. The orthorhombic zigzag distortion in $EuMnSb_2$ opens a sizable gap of ~0.5 eV at this pristine Dirac point on the Γ–M line and generates a highly dispersive linear band at Y point. The band structure of $EuMnSb_2$ is similar to the results in $CaMnSb_2$[38] with Sb zigzag chain, which has the same space group ($Pnma$) as $EuMnSb_2$. Considering a strong SOC, the band structure of $CaMnSb_2$ with Sb zigzag chains could still show a Dirac-like linear dispersion around Y point with a small band gap, which is supported by the quantum oscillation experiment and ARPES measurement[34,38]. Furthermore, massive Dirac fermion has also been revealed in similar family materials with Sb zigzag chains,
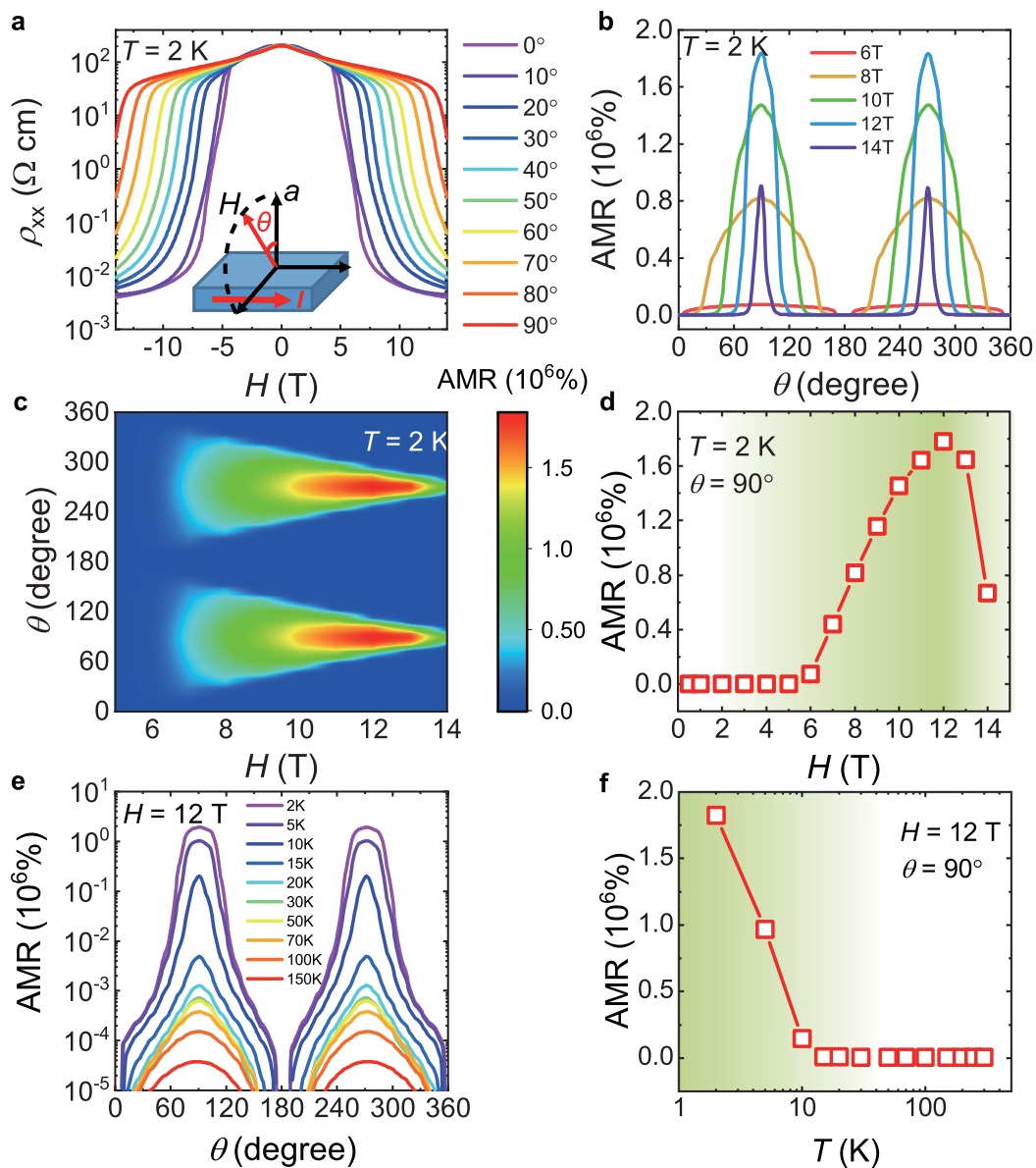
Fig. 2 AMR of EuMnSb$_2$. a Resistivity with magnetic field rotating from the a axis to the bc plane at 2 K. Inset: sketch of magneto-transport measurement geometries. The electric current is applied in the bc plane and the magnetic field is rotated from the a axis to the basal plane with keeping perpendicular to the current. The angle θ is measured from the a axis to the magnetic field direction. **b** Angular-dependent AMR (defined as AMR $= [\rho_{xx}(\theta) - \rho_{xx}(0°)]/\rho_{xx}(0°)$) at 2 K under representative magnetic fields. Here, the direction that we define as 0° has an offset about 5° from the a axis, which probably originates from the misalignment between the crystal axis of sample with the rotator. **c** Color plot of AMR map at 2 K under magnetic field between 5 and 14 T. **d** Magnetic field dependence of AMR value of 90° at 2 K. It increases rapidly with increasing magnetic field up to ~ 5 T, and shows a maximum at 12 T. **e** Evolution of AMR with the angle between the a axis and magnetic field of 12 T at various temperatures. **f** AMR value obtained at 90° as a function of temperature under 12 T. It shows relatively small value above the AFM transition temperature T_N of Eu sublattice.

including SrMnSb$_2$[33] and BaMnSb$_2$[35,36]. Therefore, a gapped Dirac cone around Y point seems to be a generic topological nature in these Mn-based 112 materials with Sb zigzag chains. Consequently, we think that EuMnSb$_2$ could be a nearly Dirac semimetal with gapped Dirac fermions. In addition, the calculations show an indirect band gap between the bottom of conductive band at Y point and the top of the valence band in the Γ–M line with 148.9 meV for the canted A-type AFM order and 125.3 meV for c-axis-oriented A-type AFM order.

Then, we also calculated the band structures with ferromagnetic (FM) order of Eu sublattice. Since the Mn sublattice forms robust C-type AFM order at much higher temperature (about 346 K)[37,44], we consider that the magnetic order of Mn^{2+} moments remains

unchanged at low temperatures with the magnetic field we have applied. In fact, magnetization measurements show that the magnetic order of Mn sublattice does not change up to 55 T in a related compound, EuMnBi$_2$[28], indicating that Mn^{2+} moments are extremely hard to be modified in this series of materials. Therefore, the magnetic structure of Mn sublattice is fixed to C-type AFM in our band structure calculations. As shown in Fig. 3d, the degenerate band in the FM state of Eu sublattice splits into spin-up and spin-down channel without SOC. The FM order has strong effect on the band around the Γ point near the Fermi level, resulting in a large splitting, while it has weak effect on the Dirac-like band at Y point. The calculated band structures considering SOC with Eu^{2+} moments ferromagnetically aligned along the a
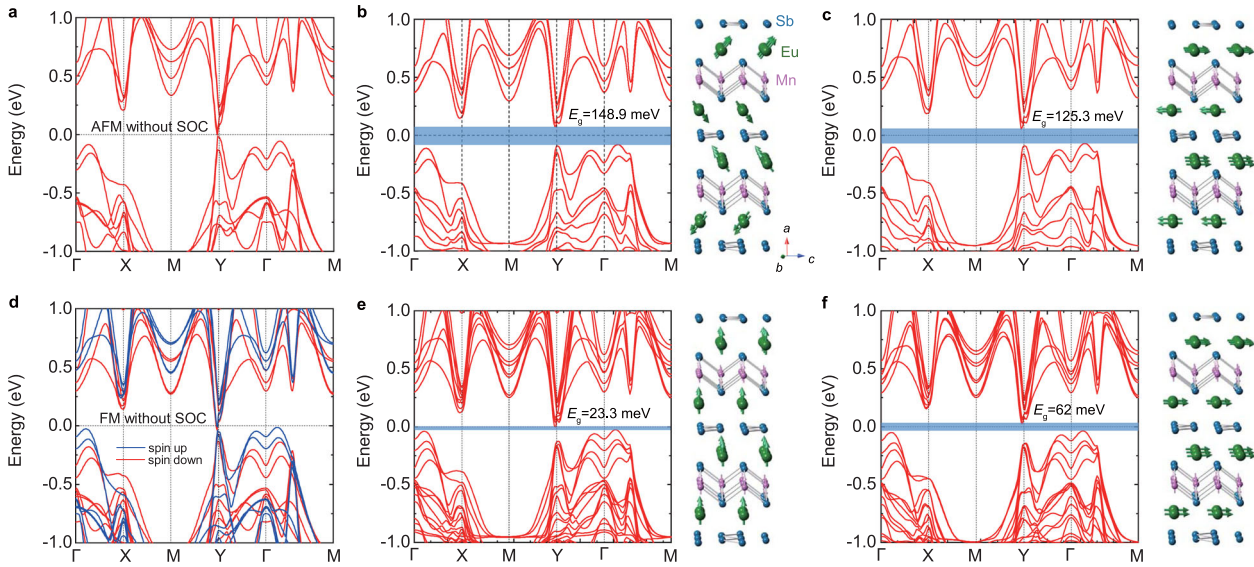
Fig. 3 Band structure of EuMnSb$_2$ with different orientations of Eu^{2+} magnetic moments. a Band structure of EuMnSb$_2$ with Eu sublattice forming AFM order without SOC. **b** Left: band structure of EuMnSb$_2$ with Eu sublattice forming canted A-type AFM order. Right: schematic illustration of the canted A-type AFM order of Eu^{2+} moments. **c** Left: band structure of EuMnSb$_2$ with Eu sublattice forming A-type AFM order with moments along the c axis. Right: schematic illustration of the of A-type AFM order of Eu^{2+} moments. **d** Band structure of EuMnSb$_2$ with Eu sublattice forming FM order without SOC. **e** Left: band structure of EuMnSb$_2$ with FM order of Eu^{2+} moments aligned along the a axis. Right: schematic illustration of the magnetic structure of Eu sublattice with FM order along the a axis. **f** Left: band structure of EuMnSb$_2$ with FM order of Eu^{2+} moments aligned along the c axis. Right: schematic illustration of the magnetic structure of Eu sublattice with FM order along the c axis.

and c axes are displayed in Fig. 3e, f, respectively. Remarkably, a strong modulation of the band structure with the ferromagnetically aligned Eu^{2+} moments is found. First, the Dirac-like band at Y point moves downward with the gap nearly unchanged. Second, the indirect band gap has a significant reduction: when the Eu^{2+} moments are aligned along the a axis, the indirect band gap reduces to 23.3 meV; when the Eu^{2+} moments are oriented in the c axis, the indirect band gap is found to be 62.0 meV, which is a bit larger than the value with Eu^{2+} moments along the a axis. The change of band structure by the spin orientation of Eu^{2+} moments in EuMnSb$_2$ leads to significant magneto-transport response. At zero field, EuMnSb$_2$ shows a relatively large band gap of ~148.9 meV, resulting in the insulating behavior of the resistivity below T_N. When the magnetic field is applied along the a axis or c axis, the Eu^{2+} moments orient toward the field direction progressively, giving rise to a large reduction of the band gap. This leads to the negative MR observed below T_N. Owing to the exchange interaction between Eu^{2+} and Mn^{2+} moments, a large magnetic field is needed to fully polarize the Eu^{2+} moments (e.g., about 22 T in EuMnBi$_2$[28]). Therefore, the MR does not saturate up to 14 T as shown in Figs. 1g and 2a, and should further increase until the Eu^{2+} moments are fully polarized. To further establish the relationship between the band gap and magnetic structure, we have calculated the band gap values based on various magnetic orders of Eu sublattice with magnetic moments oriented θ away from the c axis in the ac plane, as shown in Supplementary Fig. 7. It is clear that the band gap continuously decreases as Eu^{2+} moments rotating from the c axis to the a axis. When the magnetic field applied along the a axis increases, the Eu^{2+} moments trend to gradually polarize along the a axis (increasing θ), giving rise to a reduction in the band gap. As all the Eu^{2+} moments are oriented along the a axis ferromagnetically ($\theta = 90°$), the smallest band gap with a value of ~23.3 meV is achieved. We note that while the heuristic calculation considers A-type AFM order with Eu^{2+} moments aligned along the c axis as the starting point, which differs from the canted A-type AFM order in real case, it serves to motivate the general evolution of band gap against external magnetic field in EuMnSb$_2$. In addition, the fitted

excitation gap with $E_A = 75.9$ meV above 200 K is smaller than the calculated band gap of 148.9 meV in canted AFM state but larger than that in field-induced AF state. This indicates that the short-range magnetic correlation in high-temperature paramagnetic state above T_N can also give rise to a reduction in the band gap, which results in the transport behavior above T_N.

DISCUSSION

We further analyze the origin of the colossal AMR in our EuMnSb$_2$ sample. The band structure calculations find anisotropic band gaps between different spin orientations: 23.3 meV with Eu^{2+} moments aligned along the a axis and 62.0 meV with Eu^{2+} moments aligned along the c axis, respectively. The rotating magnetic field from the a axis to the c axis enforces the orientation of the Eu^{2+} moments, resulting in different band gap values. Such anisotropic band gap combined with corresponding position of Fermi level can result in the colossal AMR. The detailed evolution of the band structure with the corresponding position of Fermi level under magnetic field is illustrated in Fig. 4. When the magnetic field is below 5 T, the Fermi level remains inside the band gap for both $H//a$ and $H//c$, which leads to a moderate negative MR effect (Fig. 2a) and almost negligible AMR effect (Fig. 2d). Due to the Fermi level inside the band gap, the spin-flop transition around 1.5 T (as shown in Fig. 1b) has no significant effect on both MR and AMR. As the applied external field above 5 T, a field-induced MIT occurs and the conduction band around Y point starts to cross the Fermi level with $H//a$ but the Fermi level still remains inside the band gap with $H//c$. Then, a significant MR effect appears only with $H//a$, but not with $H//c$ (see a fast drop of resistivity with $H//a$ in Fig. 2a), which leads to a colossal AMR effect. When the applied external field further increases above 12 T, the conduction band around Y point also moves near the Fermi level with $H//c$. Then, a significant MR effect also appears with $H//c$, which leads to the decreasing of AMR effect above 12 T (Fig. 2d). Considering the electric neutrality of the system, the top of the valence band around Γ point should concurrently cross the Fermi level when the conduction band at Y point crosses the Fermi level. This naturally generates both
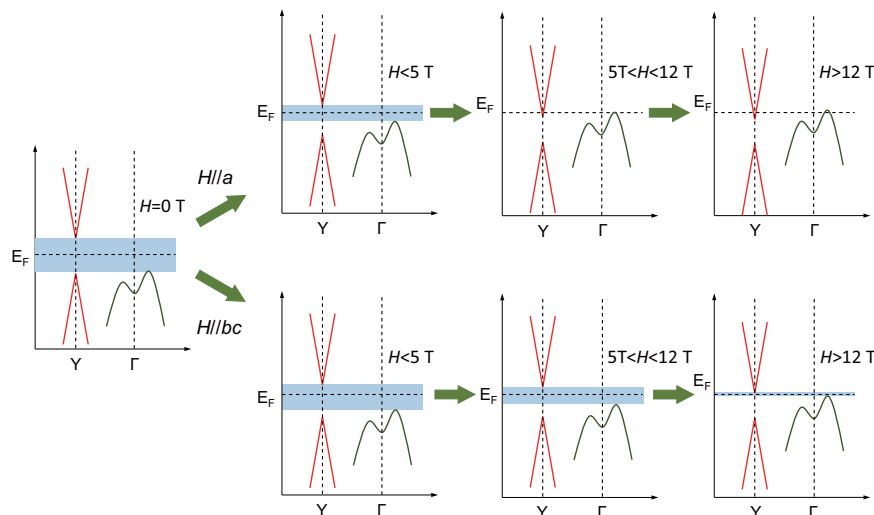
Fig. 4   The evolution of band structure and corresponding Fermi level under magnetic field. EuMnSb$_2$ shows an indirect band gap at zero magnetic field. When the applied magnetic field is below 5 T, the Fermi level remains inside the band gap with both $H//a$ and $H//c$. As the applied field increases above 5 T, the conduction band around Y point starts to cross the Fermi level with $H//a$, however, the Fermi level with $H//c$ still remains inside the band gap. When the applied field further increases above 12 T, the conduction band around Y point also moves near the Fermi level with $H//c$.

electron-type and hole-type carriers in our EuMnSb$_2$ sample and the Dirac-like electron-type carriers with high mobility dominate the transport, as revealed by the Hall data. The band structure calculation is consistent with our picture qualitatively.

Based on the above picture, we generalize that there are two key factors to account for the above colossal AMR effect. One is the magnetic-structure-induced anisotropic reduction of band gap, which essentially arises from the strongly SOC-sensitive Dirac-like band structure at Y point. The strong SOC effect results in an anisotropic band structure response to the different directions of Eu^{2+} moments under magnetic field. The other is that the conduction band should cross the Fermi level during the anisotropic reduction of band gap by applying magnetic field, which actually leads to a characteristic behavior for MIT in resistivity. These two factors also offer a natural explanation on the different behaviors between our sample and the samples used in previous reports. The zero-field resistivity of our EuMnSb$_2$ sample shows a different low-temperature behavior from that in previous reports, as shown in Supplementary Fig. 8. In previously reported EuMnSb$_2$ grown by flux or floating-zone method[37,43,44], the low-temperature resistivity shows a metallic or weakly insulating behavior. However, in our EuMnSb$_2$ single crystal, there is a strongly insulating behavior at low temperature, especially below T_N. Then, the value of resistivity at 2 K in our samples becomes almost three orders of magnitude larger than that in literatures. Our EuMnSb$_2$ sample has much lower carrier density of 9.67×10^{17} cm^{-3} (as shown in Supplementary Fig. 9) than the value $\sim 3.8 \times 10^{18}$ cm^{-3} given in the previous report[43]. Consequently, we attribute such difference in resistivity to the unintentional carrier doping induced by the impurity from Sn contamination (possibly Sn substituted on Sb atomic site) and/or Mn vacancy in previously reported samples. The energy-dispersive X-ray spectrometer (EDX) results reveal that there is no Sn contamination and less vacancy in our EuMnSb$_2$ samples (as shown in Supplementary Table 1). The low doping level makes the Fermi level locate in the band gap in our sample and the measured temperature-dependent resistivity shows insulating behavior below T_N. However, the Fermi level lies near or intersect the band edge due to the higher carrier density in previously reported EuMnSb$_2$[37,43,44], thus causing weakly insulating resistivity behavior with a drop or upturn behavior at low temperature and a much smaller MR values with weak MIT feature[37,43,44]. More importantly, our Hall resistivity indicates that

the carriers in our EuMnSb$_2$ are electron-type (Supplementary Fig. 9), which is different from the hole carrier in the previous report[43]. The different carrier type indicates that the AMR effect comes from the different mechanism between our EuMnSb$_2$ sample and previously reported samples. The dominant electron-type carrier in our EuMnSb$_2$ sample coming from the Y point is strongly affected by the SOC. Thus, our EuMnSb$_2$ can show significantly anisotropic band structure under different magnetic field directions due to the strong SOC effect on the Dirac-like electron-type carrier, which causes the colossal AMR effect. However, the hole-type carrier in previously reported EuMnSb$_2$[43] mainly comes from the top of the valance band along the Γ–M line with a weak SOC effect, but strongly affected by the spin splitting due to the FM order of Eu sublattice, which shows weakly anisotropic band structure response. Consequently, previously reported EuMnSb$_2$ is weakly affected by the SOC, thus showing a moderate AMR effect with relatively smaller value.

In conclusion, we have observed a colossal AMR reaching $\sim 1.84 \times 10^6$% at 2 K and field-induced MIT in a nearly Dirac semimetal EuMnSb$_2$ with an AFM order of Eu^{2+} moments. The external magnetic field can significantly modify the band structure at Y point near the Fermi level, which is strongly dependent on SOC and magnetism. Our work establishes magnetic topological materials as an excellent candidate to realize strong response of magneto-transport properties to the magnetism. The revealed mechanism for colossal AMR in the present study could be widely used to the topological materials in which Dirac-like fermions is strongly modulated by SOC and antiferromagnetism, which is important for the application of topological materials on spintronics. For the further room-temperature spintronic applications, it is important to find a magnetic system which manifests both strong SOC and topological properties at high temperatures, since most topological materials fail to show the "topological" characters at room temperature due to the relatively low Fermi energy compared to the level of thermal fluctuations.

METHODS

Crystal growth and characterization

EuMnSb$_2$ single crystals used in this study were grown by using Sn flux method. A mixture of Eu slugs (99.9%), Mn pieces (99.99%), Sb slugs (99.999%), and Sn shots (99.999%) in a molar ratio of 1:1:3:10 was loaded in

an alumina crucible and sealed in an evacuated quartz tube under vacuum. The quartz tube was heated slowly to 1000 °C and held for 10 h to homogenize the melt. Then it was cooled down to 600 °C at a rate of 4 °C/h, where the flux was decanted using a centrifuge. The compositions of crystals were determined using an EDX mounted on the field emission scanning electronic microscope (FESEM), Sirion200. The single-crystal XRD pattern was obtained by the X-ray diffractometer (SmartLab-9, Rigaku Corp.) with Cu Kα radiation and a fixed graphite monochromator.

Electrical transport and magnetic measurements

Electric transport measurements were carried out by using Quantum Design PPMS-14 equipped with a rotator module. Resistivity was measured using standard four-probe method and Hall resistivity was measured by standard Hall bar configuration. The rotation measurement was performed by using a commercial rotator in PPMS-14. Magnetization measurements were performed using Quantum Design MPMS-7.

Density functional calculations

Spin-polarized DFT + U calculations were performed within the Vienna ab initio Simulation Package (VASP)[52]. The generalized gradient approximation (GGA)[53] and the Perdew-Burke-Ernzerh (PBE)[53,54] of exchange-correlation functional were used. The electron–ion interaction was described with the projector augmented wave (PAW) method and Eu (4 f, 5 s, 5 p, 6 s), Mn (3 d, 4 s), and Sb (5 s, 5 p) electrons were treated as valence states. An effective Hubbard $U = 5$ eV in the GGA + U scheme[55] was applied to the localized f (Eu) and d (Mn) electrons, and the SOC interactions were also taken into account in the DFT calculations.

DATA AVAILABILITY

The data that support the findings of this study are available from the corresponding authors upon reasonable request.

CODE AVAILABILITY

The computer codes used to carry out the DFT calculations used in this work are available from the corresponding authors upon reasonable request.

REFERENCES

1. Baltz, V. et al. Antiferromagnetic spintronics. *Rev. Mod. Phys.* **90**, 015005 (2018).
2. Jungwirth, T., Marti, X., Wadley, P. & Wunderlich, J. Antiferromagnetic spintronics. *Nat. Nanotechnol.* **11**, 231–241 (2016).
3. Jungwirth, T. et al. The multiple directions of antiferromagnetic spintronics. *Nat. Phys.* **14**, 200–203 (2018).
4. Železný, J. et al. Spin transport and spin torque in antiferromagnetic devices. *Nat. Phys.* **14**, 220–228 (2018).
5. Marti, X. et al. Room-temperature antiferromagnetic memory resistor. *Nat. Mater.* **13**, 367–374 (2014).
6. Kriegner, D. et al. Multiple-stable anisotropic magnetoresistance memory in antiferromagnetic MnTe. *Nat. Commun.* **7**, 11623 (2016).
7. Park, B. G. et al. A spin-valve-like magnetoresistance of an antiferromagnet-based tunnel junction. *Nat. Mater.* **10**, 347–351 (2011).
8. Fina, I. et al. Anisotropic magnetoresistance in an antiferromagnetic semi-conductor. *Nat. Commun.* **5**, 4671 (2014).
9. Galceran, R. et al. Isothermal anisotropic magnetoresistance in antiferromagnetic metallic IrMn. *Sci. Rep.* **6**, 35471 (2016).
10. Wadley, P. et al. Electrical switching of an antiferromagnet. *Science* **351**, 587–590 (2016).
11. Wang, H. et al. Giant anisotropic magnetoresistance and nonvolatile memory in canted antiferromagnet Sr_2IrO_4. *Nat. Commun.* **10**, 2280 (2019).
12. Shick, A. B. et al. Spin–orbit coupling induced anisotropy effects in bimetallic antiferromagnets: a route toward antiferromagnetic spintronics. *Phys. Rev. B* **81**, 212409 (2010).
13. Ciccarelli, C. et al. Spin gating electrical current. *Appl. Phys. Lett.* **101**, 122411 (2012).
14. Wunderlich, J. et al. Coulomb blockade anisotropic magnetoresistance effect in a (Ga,Mn)As signle-electron transistor. *Phys. Rev. Lett.* **97**, 077201 (2006).
15. Lu, C. et al. Revealing controllable anisotropic magnetoresistance in spin–orbit coupled antiferromagnet Sr_2IrO_4. *Adv. Funct. Mater.* **28**, 1706589 (2018).
16. Baibich, M. N. et al. Giant magnetoresistance of (001)Fe/(001)Cr magnetic superlattices. *Phys. Rev. Lett.* **61**, 2472 (1988).
17. Binasch, G., Grünberg, P., Saurenbach, F. & Zinn, W. Enhanced magnetoresistance in layered magnetic structures with antiferromagnetic interlayer exchange. *Phys. Rev. B* **39**, 4828 (1989).
18. Manna, K. et al. Heusler, Weyl and Berry. *Nat. Rev. Mater.* **3**, 244–256 (2018).
19. Xu, Y. et al. High-throughput calculations of magnetic topological materials. *Nature* **586**, 702–707 (2020).
20. Wang, L. et al. Single pair of Weyl fermions in the half-metallic semimetal $EuCd_2As_2$. *Phys. Rev. B* **99**, 245147 (2019).
21. Zhang, D. et al. Topological axion states in the magnetic insulator $MnBi_2Te_4$ with the quantized magnetoelectric effect. *Phys. Rev. Lett.* **122**, 206401 (2019).
22. Xu, Y. et al. Higher-order topology of the axion insulator $EuIn_2As_2$. *Phys. Rev. Lett.* **122**, 256402 (2019).
23. Park, J. et al. Anisotropic Dirac fermions in a Bi net of $SrMnBi_2$. *Phys. Rev. Lett.* **107**, 126402 (2011).
24. Lee, G., Farhan, M. A., Kim, J. S. & Shim, J. H. Anisotropic Dirac electronic structures of $AMnBi_2$ ($A =$ Sr, Ca). *Phys. Rev. B* **87**, 245104 (2013).
25. Wang, K. et al. Quantum transport of two-dimensional Dirac fermions in $SrMnBi_2$. *Phys. Rev. B* **84**, 220401(R) (2011).
26. Wang, K. et al. Two-dimensional Dirac fermions and quantum magnetoresistance in $CaMnBi_2$. *Phys. Rev. B* **85**, 041101(R) (2012).
27. Li, L. et al. Electron–hole asymmetry, Dirac fermions, and quantum magnetore-sistance in $BaMnBi_2$. *Phys. Rev. B* **93**, 115141 (2016).
28. Masuda, H. et al. Quantum Hall effect in a bulk antiferromagnet $EuMnBi_2$ with magnetically confined two-dimensional Dirac fermions. *Sci. Adv.* **2**, e1501117 (2016).
29. Wang, A. et al. Magnetoresistance study of Dirac fermions in $YbMnBi_2$ anti-ferromagnet. *Phys. Rev. B* **94**, 165161 (2016).
30. Huang, S. et al. Nontrivial Berry phase in magnetic $BaMnSb_2$ semimetal. *Proc. Natl Acad. Sci. USA* **114**, 6256–6261 (2017).
31. Wang, Y., Xu, S., Sun, L. & Xia, T. Quantum oscillations and coherent interlayer transport in a new topological Dirac semimetal candidate $YbMnSb_2$. *Phys. Rev. Matter* **2**, 021201(R) (2018).
32. Farhan, M. A., Lee, G. & Shim, J. H. $AEMnSb_2$ ($AE =$ Sr, Ba): a new class of Dirac materials. *J. Phys. Condens. Matter* **26**, 042201 (2014).
33. Liu, J. Y. et al. A magnetic topological semimetal $Sr_{1-y}Mn_{1-z}Sb_2$ ($y,z < 0.1$). *Nat. Mater.* **16**, 905–910 (2017).
34. He, J. B. et al. Quasi-two-dimensional massless Dirac fermions in $CaMnSb_2$. *Phys. Rev. B* **95**, 045128 (2017).
35. Sakai, H. et al. Bulk quantum Hall effect of spin-valley coupled Dirac fermions in the polar antiferromagnet $BaMnSb_2$. *Phys. Rev. B* **101**, 081104(R) (2020).
36. Liu, J. Y. et al. Spin-valley locking, bulk quantum Hall effect and chiral surface state in a noncentrosymmetric Dirac semimetal $BaMnSb_2$. *Nat. Commun.* **12**, 4062 (2021).
37. Soh, J.-R. et al. Magnetic and electronic structure of Dirac semimetal candidate $EuMnSb_2$. *Phys. Rev. B* **100**, 174406 (2019).
38. Rong, H. et al. Electronic structure examination on the topological properties of $CaMnSb_2$ by angle-resolved photoemission spectroscopy. *Phys. Rev. B* **103**, 245104 (2021).
39. Sapkota, A. et al. Signatures of coupling between spin waves and Dirac fermions in $YbMnBi_2$. *Phys. Rev. B* **101**, 041111 (R) (2020).
40. Guo, Y. et al. Coupling of magnetic order to planar Bi electrons in the anisotropic Dirac metals $AMnBi_2$ ($A =$ Sr, Ca). *Phys. Rev. B* **90**, 075120 (2014).
41. Zhang, Q. et al. Influence of magnetism on Dirac semimetallic behavior in non-stoichiometric $Sr_{1-y}Mn_{1-z}Sb_2$ ($y \sim 0.07$, $z \sim 0.02$). *Phys. Rev. B* **100**, 205105 (2019).
42. Zhang, A. et al. Interplay of Dirac electrons and magnetism in $CaMnBi_2$ and $SrMnBi_2$. *Nat. Commun.* **7**, 13833 (2016).
43. Yi, C. et al. Large negative magnetoresistance of a nearly Dirac materials: layered antimonide $EuMnSb_2$. *Phys. Rev. B* **96**, 205103 (2017).
44. Gong, D. et al. Canted Eu magnetic structure in $EuMnSb_2$. *Phys. Rev. B* **101**, 224422 (2020).
45. Wang, G. et al. Field-induced metal-insulator transition in β-EuP_3. *Chin. Phys. Lett.* **37**, 107501 (2020).
46. Yin, J. et al. Large negative magnetoresistance in the antiferromagnet rare-earth dichalcogenide $EuTe_2$. *Phys. Rev. Matter* **4**, 013405 (2020).
47. Rosa, P. et al. Colossal magnetoresistance in a nonsymmorphic antiferromagnetic insulator. *npj Quantum Mater.* **5**, 52 (2020).
48. Süllow, S. et al. Magnetotransport in the low carrier density ferromagnet EuB_6. *J. Appl. Phys.* **87**, 5591–5593 (2000).
49. McGuire, T. R. & Potter, R. I. Anisotropic magnetoresistance in ferromagnetic 3d alloys. *IEEE Trans. Magn.* **11**, 1018–1038 (1975).

50. Walter, J. et al. Giant anisotropic magnetoresistance in oxygen-vacancy-ordered epitaxial La$_{0.5}$Sr$_{0.5}$CoO$_{3-\delta}$ films. *Phys. Rev. Mater.* **4**, 091401 (R) (2020).
51. Borisenko, S. et al. Time-reversal symmetry breaking type-II Weyl state in YbMnBi$_2$. *Nat. Commun.* **10**, 3424 (2019).
52. Kresse, G. & Joubert, D. From ultrasoft pseudopotentials to the projector augmented-wave method. *Phys. Rev. B* **59**, 1758–1775 (1999).
53. Perdew, J. P., Burke, K. & Ernzehof, M. Generalized gradient approximation made simple. *Phys. Rev. Lett.* **77**, 3865–3868 (1996).
54. Blöchl, P. E. Projector augmented-wave method. *Phys. Rev. B* **50**, 17953–17979 (1994).
55. Dudarev, S. L. et al. Electron-energy-loss spectra and the structural stability of nickel oxide: an LSDA + U study. *Phys. Rev. B* **57**, 1505 (1998).

ACKNOWLEDGEMENTS

AUTHOR CONTRIBUTIONS

X.H.C. conceived the project and supervised the overall research. A.F.W. and X.Y.Z. grew EuMnSb$_2$ single crystals. Z.L.S. performed the electrical transport and magnetism measurements with the help of A.F.W. and H.H.W.; H.M.M. and Z.F.W. provided ab initial band structure calculations. X.H.C., T.W., Z.Y.W., and Z.L.S. wrote the paper and all authors commented on manuscript.

COMPETING INTERESTS

The authors declare no competing interests.

ADDITIONAL INFORMATION

Supplementary information The online version contains supplementary material available at https://doi.org/10.1038/s41535-021-00397-4.

Correspondence and requests for materials should be addressed to X. Y. Zhou or X. H. Chen.

Reprints and permission information is available at http://www.nature.com/reprints

Publisher's note Springer Nature remains neutral with regard to jurisdictional claims in published maps and institutional affiliations.